Theory of the oscillatory instability of a rigid tip scraped over a polymer surface

R. Mark Bradley and Patrick D. Shipman

Phys. Rev. E **106**, 054803 — Published 17 November 2022

DOI: 10.1103/PhysRevE.106.054803

Theory of the oscillatory instability of a rigid tip scraped over a polymer surface

R. Mark Bradley

Departments of Physics and Mathematics,

Colorado State University, Fort Collins, CO 80523, USA

Patrick D. Shipman

Department of Mathematics and School of Advanced Materials Discovery,

Colorado State University, Fort Collins, CO 80523, USA

(Dated: October 17, 2022)

Abstract

The patterns produced by dragging an atomic force microscope (AFM) tip over a polymer surface are studied using a mesoscopic model introduced by Gnecco and coworkers (E. Gnecco *et al.*, New J. Phys. **17**, 032001 (2015)). We show that the problem can be reduced to solving a closed integro-differential equation for a single degree of freedom, the position of the AFM tip. We find the steady-state solution to this equation and then carry out a linear stability analysis of it. The steady state is only stable if the dimensionless indentation rate α is less than a critical value α_c which depends on dimensionless velocity of the rigid support r. Conversely, for $\alpha > \alpha_c$, periodic stick-slip motion sets in after a transient. Simulations show that the amplitude of these oscillations is proportional to $(\alpha - \alpha_c)^{1/2}$ for α just above α_c. Our analysis also yields a closed equation that can be solved for the critical value $\alpha_c = \alpha_c(r)$. If the steady-state motion is perturbed, as long the deviation from the steady state is small, the deviation of the tip's position from the steady state can be written as a linear superposition of terms of the form $\exp(\lambda_k t)$, where the complex constants λ_k are solutions to an integral equation. Finally, we demonstrate that the results obtained for the two-dimensional model of Gnecco *et al.* carry over in a straightforward way to the generalization of the model to three dimensions.

I. INTRODUCTION

Quite a number of experiments have shown that when an atomic force microscope (AFM) tip is rastered over an initially flat polymer surface in contact mode, nanoscale surface ripples form [1–11]. The AFM tip produces viscoplastic flow in the polymer as it indents the surface, and so it reshapes the surface as it moves along it. The ripples are found to have a wavelength comparable to the size of the AFM tip, and their wave vector is oriented at an oblique angle to the scan direction.

The main features of the experimentally observed ripple patterns have recently been reproduced in simulations of a phenomenological mesoscopic model [12, 13]. This model was originally introduced by Gnecco *et al.* to study a simpler problem: the pattern formed by scanning the AFM tip through a single line [9]. Clearly, the first step toward a deeper understanding of the ripples formed by scanning the tip over multiple parallel lines is to better understand what happens when a single line is scanned.

If an AFM tip rests on a polymer surface and a constant normal force $\mathcal{F}_n$ is applied to it, the surface is indented as the polymer flows and the tip progressively moves deeper and deeper into the solid. On the other hand, if the tip is dragged across the surface and $\mathcal{F}_n$ is sufficiently large, periodic stick-slip motion occurs [9, 12, 13]. The tip indents the surface and its lateral motion is slow during the "stick" phase of the motion. At the same time, the elastic energy stored in the cantilever builds. Slip then suddenly takes place. During this phase of the motion, the tip's lateral motion is rapid, most of the elastic energy in the cantilever is released, and little indentation occurs. Another stick phase then ensues. After a transient, the height of the surface behind the moving tip is a periodic function of position.

If the normal force $\mathcal{F}_n$ on the AFM tip is small, stick-slip motion does not occur. Instead, a steady state is approached in which the tip simply moves with a constant velocity. If $\mathcal{F}_n$ is increased, however, at some point a critical value of $\mathcal{F}_n$ is exceeded, an instability occurs, and stick-slip motion sets in. The model introduced by Gnecco *et al.* in Ref. [9] exhibits just such an instability. Gnecco and coworkers carried out simulations of their model and then compared the results with experiments on contact-mode AFM scanning of a polystyrene surface. The simulations agreed well with the experiments.

In this paper, we study the model of Gnecco *et al.* [9] in greater detail using a combination of analytical work and simulations. The focus of our investigation is the pattern produced by

a single line scan. To begin, we derive a closed integro-differential equation for the position of the AFM tip and show that once this equation of motion (EOM) has been solved, the surface morphology can be determined. From a physical standpoint, this means that the system consisting of the tip and surface — which would appear at first to have an infinite number of degrees of freedom — in fact has a single degree of freedom. We find the steady-state solution to the EOM and then carry out a linear stability analysis of this solution. This yields a closed equation that can be solved for the critical value of $\mathcal{F}_n$. If the steady-state motion is perturbed, so long the deviation from the steady state is small, the deviation of the tip's position from the steady state can be written as a linear superposition of terms of the form $\exp(\lambda_k t)$, where the complex constants λ_k are solutions to an integral equation. Thus, provided it is small, the deviation of the tip's position from the steady state is a sum of sinusoidally oscillating terms with exponentially increasing or decaying amplitudes. For $\mathcal{F}_n$ greater than the critical value $\mathcal{F}_{n,c}$, after a transient, there are persistent oscillations of the tip position about the steady state — this is stick-slip motion. Our simulations show that the amplitude of these oscillations grows as $(\mathcal{F}_n - \mathcal{F}_{n,c})^{1/2}$ for $\mathcal{F}_n$ just above $\mathcal{F}_{n,c}$. In addition, a pair of λ_k's that are complex conjugates of each other have a real part that changes sign from negative to positive as $\mathcal{F}_n$ is increased through its critical value. Thus, the transition from steady-state to stick-slip motion is a supercritical Hopf bifurcation.

This paper is organized as follows. In Sec. II, the two-dimensional (2D) model of Gnecco *et al.* is described. We recast the problem in dimensionless form in Sec. III and then derive the closed integro-differential equation for the position of the AFM tip. We find the steady-state solution and carry out a linear stability analysis of it in Sec. IV. In Sec. V, we carry out simulations of the model. These confirm many of the predictions of the analytical work presented in Sec. IV and yield the amplitude of the steady-state oscillation just above the transition to stick-slip motion. The generalization of the model of Gnecco *et al.* to three dimensions (3D) is briefly discussed in Sec. VI, and it is shown that results obtained for the 2D model carry over in a straightforward fashion to 3D.

II. MODEL

We will primarily study the 2D model introduced by Gnecco *et al.* in Ref. [9]. Let $x_0(t)$ denote the position of the AFM tip's apex at time t, and let $u(x,t)$ be the height of the solid

surface above the point x on the x axis at time t. In the model of Gnecco *et al.*, the motion of the AFM tip is entirely dissipative and is given by

$$\Gamma \dot{x}_0(t) = \mathcal{F}, \tag{1}$$

where Γ is a damping coefficient and $\mathcal{F}$ is the total lateral force on the tip. This force is given by

$$\mathcal{F} = -\frac{\partial U}{\partial x}(x_0(t), t), \tag{2}$$

where the potential $U = U(x,t)$ is the sum of two terms: the cantilever spring energy U_s and the surface interaction potential U_i. Explicitly,

$$U_s(x,t) = \frac{1}{2}k(x - v_0 t)^2, \tag{3}$$

where k is the spring constant and $v_0 t$ is the position of the rigid support at time t. The surface interaction potential

$$U_i(x,t) = au(x,t) \tag{4}$$

describes the tendency of the tip to move downward on the surface. Here a is a positive constant. Combining Eqs. (1) - (4), we obtain

$$\Gamma \dot{x}_0(t) = -au_x(x_0(t), t) + k[v_0 t - x_0(t)], \tag{5}$$

where the subscript on u denotes a partial derivative.

The time evolution of the surface height is given by

$$u_t(x,t) = -f(x - x_0(t)), \tag{6}$$

where once again the subscript on u denotes a partial derivative. The function $f(x)$, which describes how the AFM tip indents the surface, depends on the shape of the tip and the normal force $\mathcal{F}_n$. In Ref. [9], $f(x)$ was taken to be the sum of three Gaussians:

$$f(x) = N \exp\left(-\frac{x^2}{2\sigma^2}\right) - \frac{1}{2}N\left[\exp\left(-\frac{(x+2\sigma)^2}{2\sigma^2}\right) + \exp\left(-\frac{(x-2\sigma)^2}{2\sigma^2}\right)\right], \tag{7}$$

where the positive constants σ and N are measures of the tip width and the indentation rate, respectively. Importantly, the value of N is an increasing function of the normal force $\mathcal{F}_n$, and so there is an implicit dependence on the latter quantity. The "tip function" f given by Eq. (7) is meant to mimic the typical footprint left by the AFM tip when it indents the polymer without scanning [9].

In this paper, in addition to the triple Gaussian (7), we will consider more general tip functions f. We assume that

$$f(x) = N\tilde{f}(x/\sigma), \tag{8}$$

where $\tilde{f}$ is dimensionless, $\tilde{f}(0) = 1$ and $\tilde{f}(\tilde{x})$ tends to zero for $\tilde{x} \to \pm\infty$. The tip function given by Eq. (7) clearly satisfies these requirements.

The initial conditions needed at the starting time $t = t_0$ are the tip location $x_0(t_0)$ and the surface height $u(x, t_0) \equiv u_0(x)$ for all x. Once the tip function and the initial conditions have been specified, the coupled dynamics of the solid surface and the AFM tip are completely determined by Eqs. (5) and (6).

We will also consider the problem in which a time-dependent lateral external force $\mathcal{F}_{\rm ext}(t)$ is applied to the tip during its motion. In this case, Eq. (5) is replaced by

$$\Gamma\dot{x}_0(t) = -au_x(x_0(t), t) + k[v_0 t - x_0(t)] + \mathcal{F}_{\rm ext}(t) \tag{9}$$

and Eq. (6) is unaltered.

In the model of Gnecco *et al.*, it is assumed that the damping is so strong that the inertia of the AFM tip is completely negligible. This damping comes in large part from interfacial friction between the AFM tip and the polymer surface. In addition, the normal force $\mathcal{F}_n$ that is applied to the AFM tip produces viscoplastic flow in the polymer as it is indented. Some of the work done on the polymer by the tip is dissipated by the internal friction within the polymer. Thus, interfacial and internal friction are included in the model, and dissipative effects are an integral part of the theory.

III. CLOSED EQUATION FOR THE TIP DYNAMICS

We introduce the dimensionless distance $\tilde{x} \equiv x/\sigma$, time $\tilde{t} = kt/\Gamma$, surface height $\tilde{u}(\tilde{x}, \tilde{t}) = au(x, t)/(k\sigma^2)$, tip position $\tilde{x}_0(\tilde{t}) = x_0(t)/\sigma$ and external force $\tilde{\mathcal{F}}_{\rm ext}(\tilde{t}) = \mathcal{F}_{\rm ext}(t)/(k\sigma)$. After dropping the tildes, the equations of motion (6) and (9) become

$$\dot{x}_0(t) = -u_x(x_0(t), t) + rt - x_0(t) + \mathcal{F}_{\rm ext}(t), \tag{10}$$

and

$$u_t(x, t) = -\alpha f(x - x_0(t)). \tag{11}$$

Here

$$r \equiv \frac{\Gamma v_0}{k\sigma} \tag{12}$$

is a dimensionless measure of the tip velocity and

$$\alpha \equiv \frac{\Gamma N a}{\sigma^2 k^2} \tag{13}$$

is a dimensionless gauge of the indentation rate.

Integration of Eq. (11) with respect to time yields

$$u(x,t) = -\alpha \int_{t_0}^{t} f(x - x_0(t'))dt' + u_0(x). \tag{14}$$

Inserting Eq. (14) into Eq. (10), we obtain

$$\dot{x}_0(t) = -\int_{t_0}^{t} F(x_0(t) - x_0(t'))dt' + rt - x_0(t) + \mathcal{F}_{\rm ext}(t) - \alpha u_0'(x_0(t)), \tag{15}$$

where $F(x) \equiv -\alpha f'(x)$. Equation (15) is a closed integro-differential equation for $x_0(t)$. If we succeed in solving it for $x_0(t)$, then the surface morphology at any time $t > t_0$ can be obtained from Eq. (14). Thus, the surface morphology is effectively "slaved" to the tip dynamics. Equation (15) also shows that an initial disturbance $u(x,t_0) = u_0(x)$ has the same effect as a position-dependent external force.

We will now specialize to the case in which the surface is initially flat and set $t_0 = -\infty$. The equation of motion (15) can be simplified by introducing the time lag $\tau \equiv t - t'$ and by setting

$$l(t) \equiv rt - r - x_0(t). \tag{16}$$

Aside from the additive constant $-r$, l is the dimensionless distance that the tip lags behind the rigid support. Equation (15) reduces to

$$\dot{l}(t) = \int_0^{\infty} F(r\tau + l(t-\tau) - l(t))d\tau - l(t) - \mathcal{F}_{\rm ext}(t). \tag{17}$$

By including the term $-r$ on the right-hand side of the definition (16), we have eliminated a constant term that would otherwise have appeared in Eq. (17).

We will now focus on the case in which there is no external force. The equation of motion is then

$$\dot{l}(t) = \int_0^{\infty} F(r\tau + l(t-\tau) - l(t))d\tau - l(t). \tag{18}$$

Equation (18) is readily solved for the trivial special case in which α vanishes. When α is zero, so is F and hence $\dot{l}(t) = -l(t)$ and

$$l(t) = l(0)e^{-t}. \tag{19}$$

IV. THE STEADY STATE AND ITS STABILITY

A. The steady-state solution

Equation (18) has a steady-state solution in which $l(t)$ is simply a constant l_0 given by

$$l_0 = \int_0^\infty F(r\tau)d\tau. \tag{20}$$

Recalling that $F(x) \equiv -\alpha f'(x)$ and $f(0) = 1$, we find that

$$l_0 = \alpha/r. \tag{21}$$

Equation (16) now yields

$$x_0(t) = rt - r - \alpha/r. \tag{22}$$

As it must, the tip moves with constant velocity $\dot{x}_0 = r$ in the steady state. This is just the velocity of the rigid support in dimensionless units. Equation (22) also shows that the dimensionless distance that the tip lags behind the rigid support in the steady state is $r + \alpha/r$. Once the dimensions have been restored, this distance is

$$D = \frac{1}{k}\left(\Gamma v_0 + \frac{Na}{v_0}\right). \tag{23}$$

As we could have anticipated, the steady-state lag D is an increasing function of the indentation rate N and a decreasing function of the spring constant k. What is perhaps surprising is that D is not a monotone function of v_0, and that it becomes large in both the $v_0 \to 0$ and $v_0 \to \infty$ limits. It is also independent of the tip width σ.

Inserting Eq. (22) into Eq. (14) and setting $u_0(x) = 0$ and $t_0 = -\infty$ as before, we obtain

$$u(x,t) = -\frac{\alpha}{r}\int_{x-x_0(t)}^\infty f(\xi)d\xi. \tag{24}$$

This equation gives the surface morphology for the steady-state solution. Notice that $u(x,t)$ depends only on $x - rt$, and so the surface profile propagates with constant velocity r without changing its form. Equation (24) also gives the surface height at points far behind the tip, u_s:

$$u_s = \lim_{t\to\infty} u(x,t) = -\frac{\alpha}{r}\int_{-\infty}^\infty f(\xi)d\xi. \tag{25}$$

If the substrate is composed of an incompressible material, $u_s = 0$. Conversely, if the material is compressible, the magnitude of u_s increases with the dimensionless indentation rate α and decreases with the dimensionless tip velocity, as one would expect.

B. Linear stability of the steady-state solution

We will next study the linear stability of the steady-state solution. To that end, we set $l(t) = l_0 + l_1(t)$, where $l_1(t)$ is assumed to be small. We discard terms of second and higher order in l_1, i.e., we linearize the equation of motion (18) about the steady-state solution. This yields

$$\dot{l}_1(t) = -l_1(t) - r^{-1} M_1 l_1(t) + \int_0^\infty F'(r\tau) l_1(t-\tau) d\tau, \tag{26}$$

where

$$M_1 \equiv r \int_0^\infty F'(r\tau) d\tau = F(\infty) - F(0). \tag{27}$$

Recall that $F(x) \equiv -\alpha f'(x)$. Following Ref. [9], we assume that $f'(x) \to 0$ as $x \to \infty$ and take $f(x)$ to be an even function of x, so that $f'(0) = f'(\infty) = 0$. We then have $M_1 = 0$.

We seek solutions to Eq. (26) of the form

$$l_1(t) = l_{1,0} \exp(\lambda t), \tag{28}$$

where λ and $l_{1,0}$ are complex constants. $l_{1,0}$ is arbitrary because Eq. (26) is linear. λ, on the other hand, must be a solution to the equation

$$\lambda = -1 + \int_0^\infty F'(r\tau) e^{-\lambda\tau} d\tau. \tag{29}$$

Suppose that the steady state is perturbed at some time by a weak external force. As we show in the Appendix, shortly after the steady state has been disturbed, the deviation from the steady state $l_1(t)$ can be written as a linear superposition of solutions of the form (28) where the λ's are solutions to Eq. (29). Therefore, if $\mathrm{Re}\,\lambda$ is negative for all solutions λ to Eq. (29), then the steady-state solution is stable. Conversely, if $\mathrm{Re}\,\lambda$ is positive for any λ, then the steady-state solution is unstable.

For convenience, we set $\Lambda \equiv \lambda/r$ and $\hat{\tau} \equiv r\tau$. Equation (29) becomes

$$r\Lambda + 1 = -\frac{\alpha}{r} \int_0^\infty f''(\hat{\tau}) e^{-\Lambda\hat{\tau}} d\hat{\tau}. \tag{30}$$

Notice that the integral that appears on the right-hand side of Eq. (30) is the Laplace transform of the second derivative of the tip function, f''. In addition, if Λ is a solution to Eq. (30), then so is its complex conjugate Λ^*. Finally, if $\alpha = 0$, then Eq. (30) has the single solution $\Lambda = -1/r$ which gives $\lambda = -1$. This is precisely the result we obtained earlier for this special case — see Eq. (19).

Consider a particular value of r that is positive. For $\alpha = 0$, Eq. (29) has a single solution, namely $\lambda = -1$. The steady state is therefore stable. If we now begin to increase α, this solution to Eq. (29) changes continuously, and additional solutions may appear. At first, all of these solutions λ_1, $\lambda_2, \ldots$ and λ_n to Eq. (29) have negative real parts, and the steady-state solution remains stable. However, for all of the tip functions we will consider, the real part of one or more of these solutions reaches zero at a critical value of α that we will denote by $\alpha_c(r)$. For $\alpha > \alpha_c(r)$, at least one of the λ's has a positive real part and the steady-state solution is therefore unstable. A stick-slip transition therefore occurs as α is increased through the critical value $\alpha_c(r)$

A value of λ that has zero real part at $\alpha = \alpha_c(r)$ must have a nonzero imaginary part. To see this, suppose the opposite were true, so that $\lambda = 0$ is a solution to Eq. (29) for $\alpha = \alpha_c(r)$. Equation (29) then reduces to

$$-1 + \int_0^\infty F'(r\tau)d\tau = 0, \tag{31}$$

where $F(r\tau) = -\alpha_c(r)f'(r\tau)$. The integral that appears in Eq. (31) is M_1/r, which we have already shown is zero. We therefore have a contradiction.

Because λ^* is a solution to Eq. (29) if λ is, an even number of λ's must have a vanishing real part for $\alpha = \alpha_c(r)$. The simplest scenario is that there is a single pair of pure imaginary λ's at the critical value of α, and this will be the case save for very unusual tip functions f. This pair of λ's must be complex conjugates of one another and so the transition from stability to instability is a Hopf bifurcation.

Suppose that $\alpha = \alpha_c(r)$ and that there is a single pair of pure imaginary λ's, $i\omega$ and $-i\omega$, where ω is real and positive. In addition, we suppose that the system is in its steady state and then the tip is briefly disturbed by a small external force. As shown in the Appendix, after the perturbation has ended, $l_1(t)$ may be written

$$l_1(t) = \sum_{j=1}^{n} A_j e^{\lambda_j t}, \tag{32}$$

where the A_j's are complex constants. Once sufficient time has passed, only the terms with pure imaginary λ_j's will make a significant contribution to $l_1(t)$ and hence to a good approximation

$$l_1(t) = Ae^{i\omega t} + \text{c.c.} \tag{33}$$

Here A is a complex constant with a value that depends on the nature of the perturbing force. Consider a point x that the tip passes long after its motion has been perturbed. The surface height at x long after the tip has passed is

$$u_\infty(x) \equiv \lim_{t\to\infty} u(x,t). \tag{34}$$

Equation (14) shows that

$$u_\infty(x) = -\alpha \int_{-\infty}^{\infty} f(x - x_0(t))dt. \tag{35}$$

Let $x_{0,s}(t) = rt - r - \alpha/r$ be the steady-state solution given by Eq. (22). Equation (35) can be written

$$u_\infty(x) = -\alpha \int_{-\infty}^{\infty} f(x - x_{0,s}(t) + l_1(t))dt. \tag{36}$$

Linearizing this about the steady state, we obtain

$$\begin{aligned} u_\infty(x) &= u_s - \alpha \int_{-\infty}^{\infty} f'(x - x_{0,s}(t))l_1(t)dt \\ &= u_s - \frac{\alpha}{r} \int_{-\infty}^{\infty} f'(\xi)l_1(r^{-1}(x - \xi + r + \alpha/r))dt. \end{aligned} \tag{37}$$

Finally, inserting Eq. (33) into this result, we obtain

$$u_\infty(x) = u_s + \mathcal{A}\cos(qx + \phi), \tag{38}$$

where the wave number $q \equiv \omega/r$ and the values of the constants $\mathcal{A}$ and ϕ depend on the nature of the perturbing force. Equation (33) shows that the tip position $x_0(t)$ oscillates sinusoidally about the steady-state position $x_{0,s}(t)$ with period $T = 2\pi/\omega$. Equation (38), on the other hand, shows that the surface height varies sinusoidally with position with wavelength $L = 2\pi r/\omega$. Naturally, these two conclusions remain approximately valid if α differs slightly from $\alpha_c(r)$.

The critical value of α is $\alpha_c(r)$ for a given value of r. Equation (30) can be used to determine $\alpha_c(r)$, and we will follow that route in Sec. IV C for a particular choice of tip function f. For other tip functions, it is best to reformulate the problem. Given r, we can try to simultaneously find values of α and $\lambda = i\omega$ that satisfy Eq. (29). However, making use of Eq. (30), this task can be reduced to solving first for ω and then for α. To see this, we first set $\Omega = \omega/r$. Equation (30) becomes

$$ir\Omega + 1 + \frac{\alpha_c(r)}{r} \int_0^{\infty} f''(\hat{\tau})\mathrm{e}^{-i\Omega\hat{\tau}}d\hat{\tau} = 0. \tag{39}$$

The real and imaginary parts of Eq. (39) are

$$1 + \frac{\alpha_c(r)}{r} \int_0^\infty f''(\hat{\tau}) \cos(\Omega\hat{\tau}) d\hat{\tau} = 0 \tag{40}$$

and

$$r\Omega - \frac{\alpha_c(r)}{r} \int_0^\infty f''(\hat{\tau}) \sin(\Omega\hat{\tau}) d\hat{\tau} = 0. \tag{41}$$

Equations (40) and (41) may be solved for r and $\alpha_c(r)$ to give

$$r = r(\Omega) = -\frac{\int_0^\infty f''(\hat{\tau}) \sin(\Omega\hat{\tau}) d\hat{\tau}}{\Omega \int_0^\infty f''(\hat{\tau}) \cos(\Omega\hat{\tau}) d\hat{\tau}}, \tag{42}$$

and

$$\alpha_c(r) = -\frac{r}{\int_0^\infty f''(\hat{\tau}) \cos(\Omega\hat{\tau}) d\hat{\tau}} = \frac{\int_0^\infty f''(\hat{\tau}) \sin(\Omega\hat{\tau}) d\hat{\tau}}{\Omega \left(\int_0^\infty f''(\hat{\tau}) \cos(\Omega\hat{\tau}) d\hat{\tau} \right)^2}. \tag{43}$$

Given r, the value of Ω may be determined numerically from Eq. (42) if it is not possible to solve for it analytically. Equation (43) then yields the value of $\alpha_c(r)$.

C. An example

We next study a relatively simple, illustrative choice of tip function: we set $f(x) = J_0(x)$, where J_0 is the Bessel function of order zero. This choice of tip function satisfies all of the assumptions we have made on the form of f and has the virtue of being analytically tractable. However, it is not expected to model a real tip function particularly well. The dynamics with more realistic tip functions will be treated numerically in Sec. V.

For $f(x) = J_0(x)$, Eq. (30) becomes

$$r\Lambda + 1 = \frac{\alpha}{r} \left(\Lambda - \frac{\Lambda^2}{\sqrt{\Lambda^2 + 1}} \right) \tag{44}$$

after some algebra. Equation (44) has the single solution $\Lambda = -1/r$ for $\alpha = 0$, as we have already noted. For positive α, Λ satisfies

$$\sqrt{\Lambda^2 + 1}[(1 - \alpha\rho^2)\Lambda + \rho] = -\alpha\rho^2\Lambda^2, \tag{45}$$

where $\rho \equiv 1/r$. (For $\alpha = 0$, Eq. (45) has the roots $\Lambda = -\rho$, i and $-i$. The latter two roots are extraneous.) There are two purely imaginary, nonzero roots of Eq. (45) for $\alpha = \alpha_c(r)$.

These will be denoted $i\omega$ and $-i\omega$, where ω is real and positive. We will now show that $\alpha_c(r) = r^2$. For $\alpha = \alpha_c(r)$, Eq. (45) becomes

$$\sqrt{1-\omega^2}\{[1-\alpha_c(r)\rho^2]i\omega + \rho\} = \alpha_c(r)\rho^2\omega^2. \tag{46}$$

There are two cases to be considered: $0 < \omega < 1$ and $\omega \geq 1$. If $0 < \omega < 1$, we take the imaginary part of Eq. (46) and so obtain $\sqrt{1-\omega^2}\{[1-\alpha_c(r)\rho^2]\omega = 0$. This gives $\alpha_c(r) = r^2$. If $\omega \geq 1$, on the other hand, taking the imaginary part of Eq. (46) yields $\rho\sqrt{1-\omega^2} = 0$ and hence $\omega = 1$. However, $\omega = 1$ is clearly not a solution to Eq. (46). We are therefore led to the conclusion that $\alpha_c(r) = r^2$. Equation (46) therefore reduces to $\rho\sqrt{1-\omega^2} = \omega^2$ which implies that

$$\omega = \left(\frac{\sqrt{1+4r^2}-1}{2r^2}\right)^{1/2}. \tag{47}$$

$\alpha_c(r) = r^2$ is an increasing function of r. This is not surprising, since we would expect that the faster the tip is dragged, the greater the indentation rate needed to produce stick-slip motion.

V. NUMERICAL SIMULATIONS

We study the dynamics through numerical integrations of the system given by Eqs. (10) and (11) with no external forcing ($\mathcal{F}_{\rm ext}(t) \equiv 0$) and a tip function of the form

$$f(x) = \exp\left(-\frac{x^2}{2}\right) - \frac{\beta}{2}\left[\exp\left(-\frac{(x+2)^2}{2}\right) + \exp\left(-\frac{(x-2)^2}{2}\right)\right]. \tag{48}$$

As seen from Eq. (11), the rate of change in volume of the material due to compression is

$$\frac{d}{dt}\int_{-\infty}^{\infty} u(x,t)dx = -\alpha\int_{-\infty}^{\infty} f(x - x_0(t))dx = -\alpha(1-\beta). \tag{49}$$

We carried out simulations for the parameter choices $\beta = 0$ and $\beta = 1$. In the latter case, there is no compression and Eq. (48) is the dimensionless form of the triple-Gaussian tip function (7) studied in Ref. [9]. The tip function $f(x)$ is a Gaussian for $\beta = 0$.

The initial state in all of our simulations was the steady-state solution for $x_0(t)$ and $u(x,t)$ evaluated at time $t = t_1$, except that spatial white noise with a maximum amplitude of 10^{-4} was added to $u(x,t_1)$. For the case of incompressible material ($\beta = 1$), the initial surface was therefore simply low-amplitude spatial white noise. So that the solutions could be nicely

displayed, the initial tip position was taken to be positive rather than zero; we somewhat arbitrarily chose $x_0(t_1) = 14$. Thus, in accord with Eq. (22), $t_1 = r^{-1}(r + \alpha r^{-1} + 14)$.

To implement the numerical simulations, the system of equations given by Eqs. (10) and (11) was converted to a system of ordinary differential equations for $N + 1$ time-dependent variables, namely the tip position $x_0(t)$ and the surface heights $u(x_j, t)$ at positions $x_j = j\Delta x$, where $1 \leq j \leq N$. The resulting system was solved using the Runge-Kutta (4,5) method (`ode45` in MATLAB) with the choice $\Delta x = 0.001$ and an adaptive time step of approximately $\Delta t = 0.04$.

To begin, we will fix the value of the dimensionless velocity of the rigid support r at 1 and vary the dimensionless indentation rate α. As we saw in Sec. IV B, for $\alpha = \alpha_c(r)$, the period of the temporal oscillation of the tip velocity is $T = 2\pi/\omega$ and the period of the spatial oscillation of $u_\infty(x)$ is $L = 2\pi r/\omega$. Therefore, T and L coincide for $r = 1$.

For $\beta = 1$, we find that Eq. (29) has the roots $\lambda = \pm 0.943\mathrm{i}$ at $\alpha = \alpha_c = 1.069$. The real part of these roots is negative (positive) for α slightly smaller (larger) than α_c and all other roots have negative real parts. The prediction, therefore, is that the steady-state solution is stable for $\alpha - \alpha_c < 1.069$ and unstable to oscillations with $T = L = 2\pi/0.943 = 6.665$ for α slightly larger than α_c. Numerical simulations confirm this prediction: Fig. 1 (top panel) shows the surface $u(x, t)$ at time $t = 361$ for $\alpha = \alpha_c - 0.01$; although there are oscillations at early times, the amplitude of the oscillations decays to zero. The analogous surface plot for $\alpha = \alpha_c + 0.01$, shown in Fig. 1 (center panel), exhibits persistent oscillations that approach a bounded amplitude. The velocity of the tip $\dot{x}_0(t)$ oscillates about the predicted mean value $r = 1$, as shown in Fig. 1 (bottom panel) for $\alpha = \alpha_c + 0.01$. As shown in Fig. 2 (left panel), the squares of the amplitudes of the periodic oscillations of $x_0(t)$ and $u(x, \cdot)$ are linearly proportional to $\alpha - \alpha_c$ for small values of $\alpha - \alpha_c$ once the system has reached a steady state. This is consistent with the prediction of a Hopf bifurcation [14]. Since a stable periodic solution develops as α is increased above α_c and the steady-state solution given by Eqs. (22) and (24) becomes unstable, the bifurcation is a supercritical Hopf bifurcation. Figure 3 (left panel) shows that the wavelength L approaches the predicted value of 6.665 as $\alpha \to \alpha_c^+$ and that the deviation of L from its value at $\alpha = \alpha_c$ is proportional to $\alpha - \alpha_c$ for small values of $\alpha - \alpha_c$. (In the original units, the wavelength of the surface pattern left behind the tip is 6.665σ in the limit that α approaches α_c from above.)

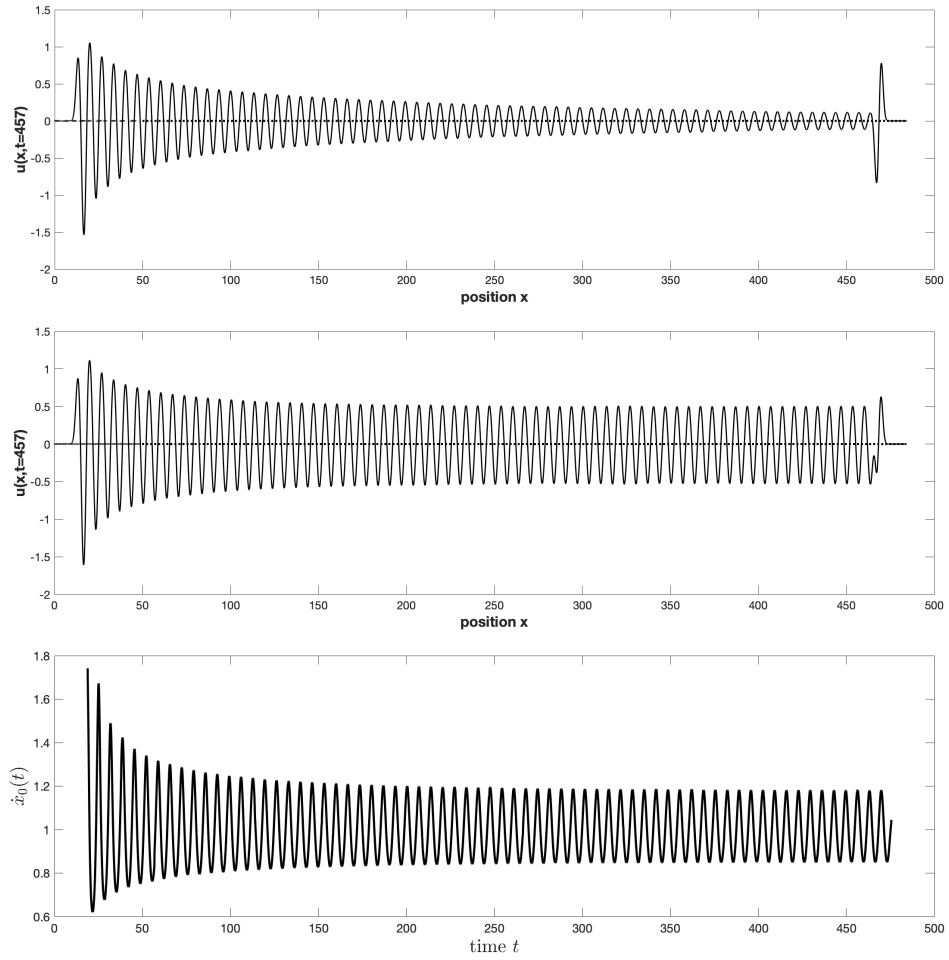

FIG. 1: Results of simulations of the system given by Eqs. (10) and (11) with $\mathcal{F}_{\text{ext}}(t) \equiv 0$, dimensionless tip velocity $r = 1$, and tip function (48) with $\beta = 1$. For $t_1 = 15 + \alpha$, the initial conditions are $x_0(t_1) = 14$, with $u(x, t_1)$ equal to the steady-state solution $u(x, t_1) \equiv 0$ plus low-amplitude spatial white noise. Shown are graphs of $u(x, t = 457)$ for $\alpha = \alpha_c - 0.01$ (top panel) and $\alpha = \alpha_c + 0.01$ (center panel), and a graph of $\dot{x}_0(t)$ for $\alpha = \alpha_c + 0.01$ (bottom panel). The critical value of α is $\alpha_c = 1.069$.

For the parameter choice $\beta = 0$, we find that for $r = 1$ Eq. (29) has the roots $\lambda = \pm 0.934\text{i}$ at $\alpha = \alpha_c = 1.608$. The linear stability analysis predicts the steady-state solution $u(x, \cdot)$ to

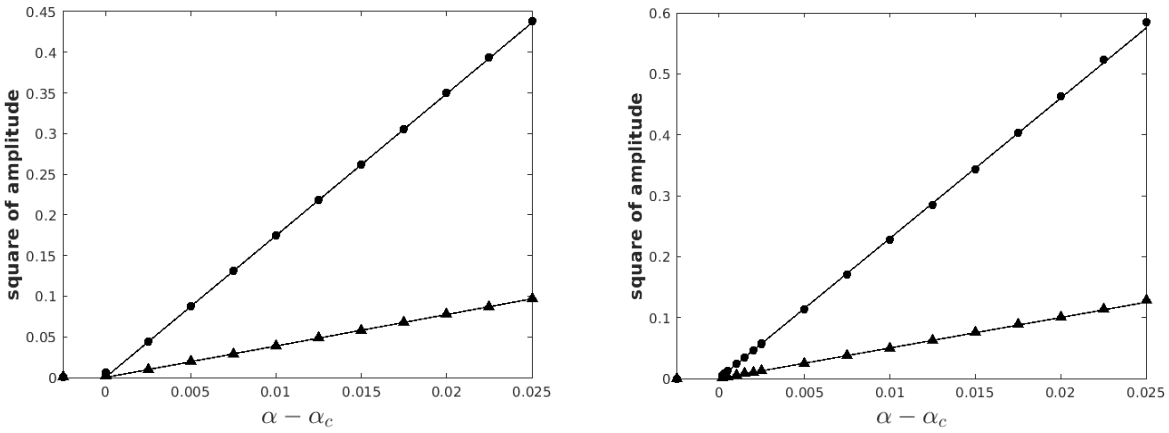

FIG. 2: The square of the amplitude of the steady-state spatial oscillation of $u(x, \cdot)$ (dots) and temporal oscillation of $x_0(t)$ (triangles) *vs.* $\alpha - \alpha_c$, found by numerical integrations of the system given by Eqs. (10) and (11) with $\mathcal{F}_{\text{ext}}(t) \equiv 0$, parameter choice $r = 1$ and tip function (48) with $\beta = 1$ (left panel) and $\beta = 0$ (right panel). For $\beta = 1$, $\alpha_c = 1.069$, and for $\beta = 0$, $\alpha_c = 1.608$. The lines of best fit to the first four data points with $\alpha > \alpha_c$ are plotted.

be stable for $\alpha - \alpha_c < 1.608$ and unstable to oscillations with $T = L = 2\pi/0.934 = 6.727$ for α just above $\alpha_c = 1.608$. Figure 4 displays the surface $u(x, t)$ at time $t = 954$ (solid line) for a simulation with $\alpha = \alpha_c + 0.03$. The dotted line shows the initial surface $u(x, t_1)$ given by Eq. (24). The amplitude of the oscillation approaches a finite value, albeit much more slowly than in the simulation with $\beta = 1$ shown in Fig. 1 (middle panel). The right panel of Fig. 2 shows that for $\beta = 0$, the squared amplitudes of the oscillations are proportional to $\alpha - \alpha_c$ for small values of $\alpha - \alpha_c$, just as they are for $\beta = 1$. Figure 3 (right panel) shows that the wavelength approaches the predicted value of 6.727 as $\alpha \to \alpha_c^+$ and that the deviation of L from its value at $\alpha = \alpha_c$ is proportional to $\alpha - \alpha_c$ for small values of $\alpha - \alpha_c$.

A transition from steady-state to stick-slip motion also occurs if the dimensionless indentation rate α is held fixed and the dimensionless tip velocity r is varied instead. Figure 5 shows the squared amplitudes of the oscillations in $x_0(t)$ and $u(x, \cdot)$ for simulations with the value of α held fixed at 1 and with $\beta = 1$. For these parameter values, Eq. (29) has roots $\lambda = \pm 0.915\text{i}$ at $r = r_c = 0.96$. The period of the temporal oscillations approaches $2\pi(0.96)/0.915 = 6.59$ as r approaches r_c from below, as predicted.

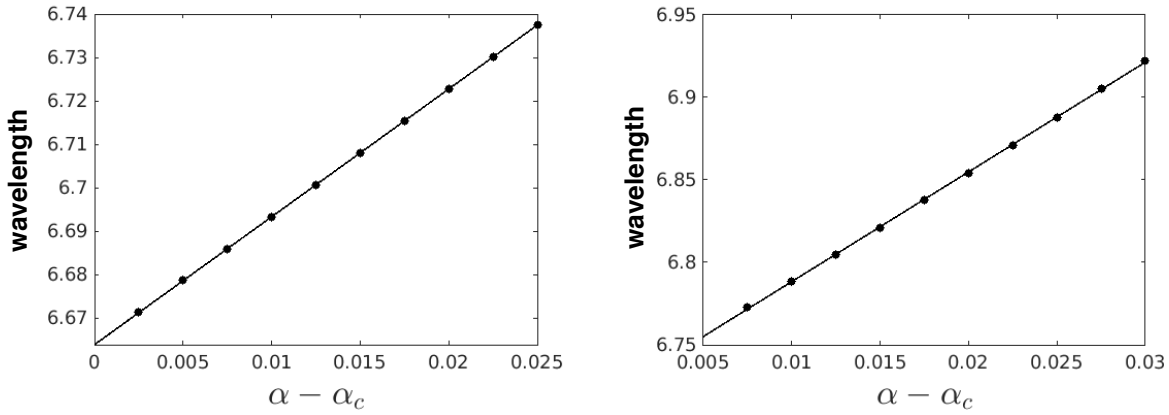

FIG. 3: The wavelength of the steady-state spatial oscillation of $u(x, \cdot)$ *vs.* $\alpha - \alpha_c$, found by numerical simulations of the system given by Eqs. (10) and (11) with $\mathcal{F}_{\text{ext}}(t) \equiv 0$, parameter choice $r = 1$ and tip function (48) with $\beta = 1$ (left panel) and $\beta = 0$ (right panel). For $\beta = 1$, $\alpha_c = 1.069$, and for $\beta = 0$, $\alpha_c = 1.608$. The lines of best fit are also plotted.

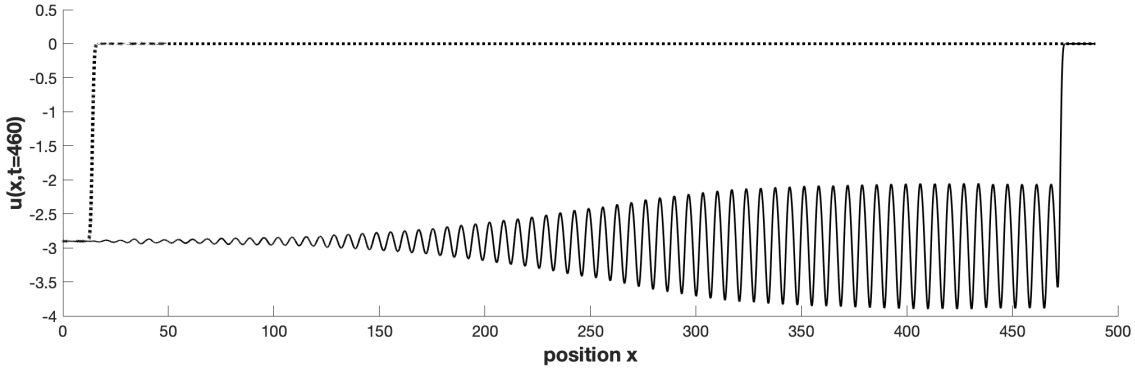

FIG. 4: The surface pattern $u(x, t = 460)$ resulting from a simulation of the system given by Eqs. (10) and (11) with $\mathcal{F}_{\text{ext}}(t) \equiv 0$, parameter choice $r = 1$ and tip function (48) with $\beta = 0$. The initial tip position was $x_0(t_1) = 14$ at time $t_1 = 15 + \alpha$. The initial surface $u(x, t_1)$, which graphed with a dotted line, is given by Eq. (24). (Low amplitude spatial white noise was added to $u(x, t_1)$ as described in the text.) The parameter α was $\alpha = \alpha_c + 0.03$, where $\alpha_c = 1.608$.

The region in (r, α) parameter space for which the steady-state solution is unstable may be determined from Eqs. (42) and (43). These expressions give, as functions of Ω, points

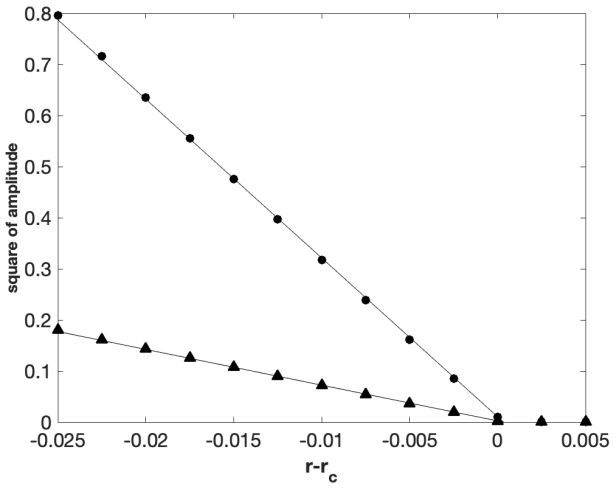

FIG. 5: The square of the amplitude of the steady-state spatial oscillation of $u(x,\cdot)$ (dots) and of the temporal oscillation of $x_0(t)$ (triangles) *vs.* $r - r_c$, found by numerical simulations of the system given by Eqs. (10) and (11) with $\mathcal{F}_{\text{ext}}(t) \equiv 0$, parameter choice $\alpha = 1$ and tip function (48) with $\beta = 1$. The critical value of r is $r_c = 0.96$. The lines of best fit to the first four data points with $r < r_c$ are plotted.

$(r(\Omega), \alpha_c(\Omega))$ on the boundary between the regions of stability and instability in (r, α) parameter space. In Fig. 6, we show the parametric curve $(r(\Omega), \alpha_c(\Omega))$ for the tip function (48) for $\beta = 1$ (left panel) and $\beta = 0$ (right panel). The steady-state solution is unstable for pairs (r, α) with $\alpha > \alpha_c(r)$. The unstable regions are shaded in the two panels.

VI. TIP DYNAMICS IN THREE DIMENSIONS

To this point, we have studied the 2D model introduced by Gnecco *et al.* [9]. Naturally, in the real world, the dynamics of the tip occurs in three dimensions rather than two. However, as we will show in this section, the dynamics in 3D can be reduced to the 2D problem we have already studied if certain conditions apply.

We begin by briefly describing the natural generalization of the model of Gnecco *et al.* to 3D. Let $u(x, y, t)$ be the height of the solid surface above the point (x, y) in the $x - y$ plane at time t. In addition, $\boldsymbol{x}_0(t) = x_0(t)\hat{\boldsymbol{x}} + y_0(t)\hat{\boldsymbol{y}}$ will denote the position of the AFM tip's

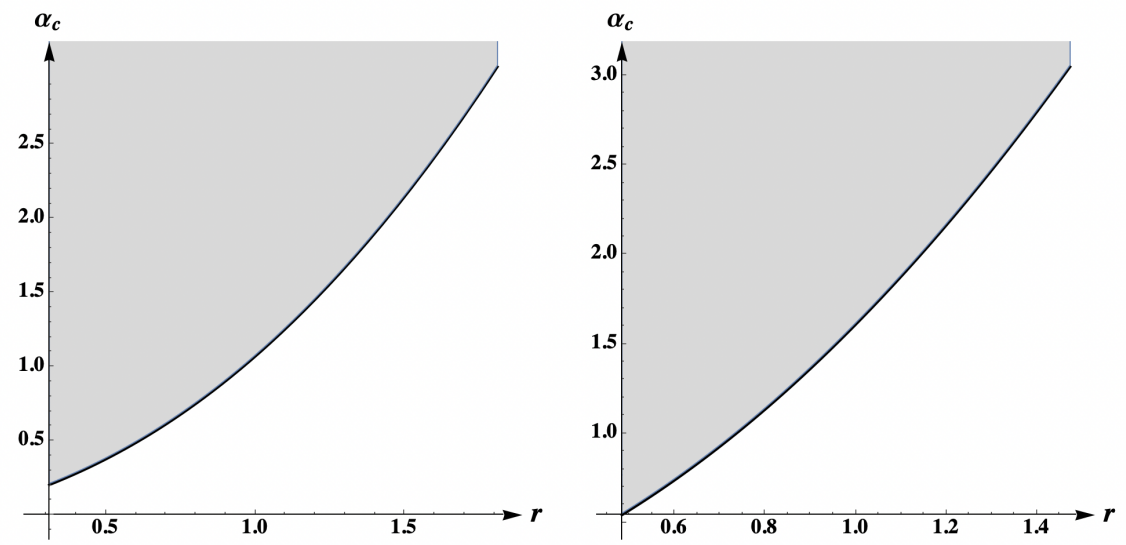

FIG. 6: The critical value of α as a function of r, $\alpha_c(r)$, for the tip function (48) for $\beta = 1$ (left panel) and $\beta = 0$ (right panel). The curves were determined from Eqs. (42) and (43) as parametric plots $(r(\Omega), \alpha_c(\Omega))$ parameterized by Ω. The steady-state solution is unstable in the region with $\alpha > \alpha_c(r)$ which is shaded in the two panels.

apex at time t projected onto the $x - y$ plane. The 3D analog of Eq. (1) is

$$\Gamma \dot{\boldsymbol{x}}_0(t) = \boldsymbol{\mathcal{F}}. \tag{50}$$

The total force $\boldsymbol{\mathcal{F}}$ on the tip is given by

$$\boldsymbol{\mathcal{F}} = -\boldsymbol{\nabla} U(x_0(t), y_0(t), t), \tag{51}$$

where $U = U_s + U_i$ as before and $\boldsymbol{\nabla} \equiv \hat{\boldsymbol{x}}\partial_x + \hat{\boldsymbol{y}}\partial_y$ denotes the 2D gradient. Equation (3) is replaced by

$$U_s(x,t) = \frac{1}{2}k(x - v_0 t)^2 + k' y^2, \tag{52}$$

where the longitudinal and transverse spring constants k and k' differ in general. The surface interaction potential is

$$U_i(x,y,t) = a u(x,y,t). \tag{53}$$

Combining Eqs. (50) - (53), we obtain

$$\Gamma \dot{x}_0(t) = -a u_x(x_0(t), y_0(t), t) + k[v_0 t - x_0(t)], \tag{54}$$

and

$$\Gamma \dot{y}_0(t) = -a u_y(x_0(t), y_0(t), t) - k' y_0(t), \tag{55}$$

The time evolution of the surface height is given by

$$u_t(x, y, t) = -f(x - x_0(t), y - y_0(t)). \tag{56}$$

where $f = f(x, y)$ is the tip function.

We assume that the tip function $f(x, y)$ is an even function of both x and y and that the tip apex initially lies above the x axis, so that $y_0 = 0$ at time $t = t_0$. In addition, we take the surface to be flat at time $t = t_0$. Nothing breaks the $y \to -y$ symmetry in this case, and so $y_0(t) = 0$ for all $t \geq t_0$.

A note of caution must be added at this point. If $f_{yy}(x, 0)$ is positive for any value of x, then the solution with $y_0(t) = 0$ could be unstable against small perturbations. This will occur if the AFM "tip" is actually two tips that are symmetrically placed relative to the y axis, for example. However, if the AFM tip has a reasonable shape, $f_{yy}(x, 0)$ will be negative for all x and the solution to the problem with $y_0(t) = 0$ will be stable. We assume that this is indeed the case.

If $y_0(t) = 0$ for all $t \geq t_0$, Eq. (54) is formally equivalent to Eq. (5). In addition, Eq. (56) gives

$$u_t(x, 0, t) = -f(x - x_0(t), 0). \tag{57}$$

which is formally identical to Eq. (6). Thus, the problem of finding $x_0(t)$ is exactly the same problem in 2D and 3D. Once $x_0(t)$ has been found for the equivalent 2D problem, Eq. (56) with $y_0(t)$ set to zero can be integrated with respect to time to give the surface morphology in 3D.

If the tip function $f(x, y) = g(x)h(y)$ is a product of a function $g(x)$ of x and a function $h(y)$ of y, the 3D surface morphology is especially simple. In that case,

$$u(x, y, t) = -h(y) \int_{t_0}^{t} g(x - x_0(t'))dt' = u_{2D}(x, t)h(y), \tag{58}$$

where $u_{2D}(x, t)$ is the solution to the 2D problem with tip function $g(x)$. Thus, the surface height $u(x, y, t)$ in the 3D problem can be obtained simply by multiplying the surface height $u_{2D}(x, t)$ in the equivalent 2D problem by $h(y)$.

The 3D analog of the 2D tip function (48) with $\beta = 0$, namely

$$f(x, y, t) = \exp\left(-\frac{x^2 + y^2}{2}\right), \tag{59}$$

satisfies the conditions. Therefore, given the solution $u(x,t)$ shown in Fig. 4, the solution of the 3D problem with tip function (59) is

$$u(x,y,t) = u(x,t)\exp\left(-\frac{y^2}{2}\right). \tag{60}$$

The surface height for the 3D problem at time $t = 460$ is shown in Figure 7.

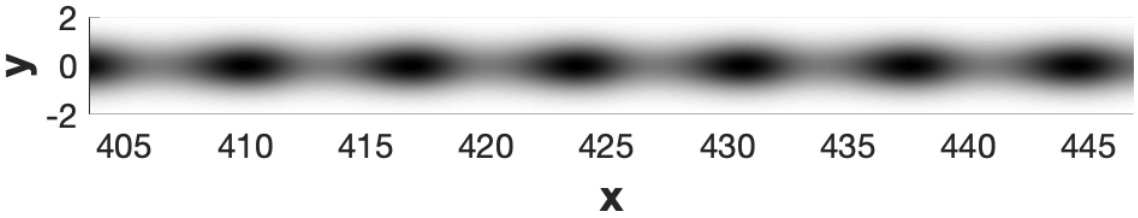

FIG. 7: Gray-scale image of $u(x,y,t=460)$ in the domain with $400 < x < 450$ and $-2 < y < 2$ for the tip function (59), constructed from the solution $u(x,t=460)$ shown in Fig. 4 using Eq. (60). Darker shading corresponds to smaller values of $u(x,y,t=460)$.

VII. DISCUSSION

As we have seen, in pioneering work, Gnecco *et al.* introduced a phenomenological model for the stick-slip motion that occurs as an AFM tip is scanned in a single line across a polymer surface [9]. This model was subsequently extended to three dimensions and was modified to mimic the slowing rate of indentation observed if the tip is not dragged across the surface [12, 13]. The resulting model gives excellent agreement with experiments in which the AFM tip is rastered in parallel lines across the surface, producing ripples [12, 13].

In this paper, we have studied the model introduced by Gnecco *et al.* in Ref. [9]. Our results on the model differ from theirs in some important respects. In particular, Gnecco and coworkers argued that an approximate criterion for the stick-slip transition for the triple Gaussian tip function (7) is $k = 1.406N/(\sigma v_0)$ [9]. Recast in terms of dimensionless quantities, their prediction is that $\alpha_c(r) = 0.7112r$. Using the exact result Eq. (29), we found that $\alpha_c = 1.069$ for $r = 1$. The value $\alpha_c = 0.7112$ given by the criterion of Gnecco *et*

al. for $r = 1$ differs widely from the correct value. In addition, the results shown in the left panel of Fig. 6 show that $\alpha_c(r)$ is not simply proportional to r.

In the simulation results given in Ref. [9], the ripple amplitude $\mathcal{A}$ appears to jump discontinuously from zero to a nonzero value as the indentation rate N is increased through its critical value. Similarly, the results of Gnecco *et al.* suggest that $\mathcal{A}$ jumps discontinuously from zero to a nonzero value as the scan velocity v_0 is reduced through its critical value. In our approach to the numerical work, the task of determining how the ripple amplitude changes in the immediately vicinity of the stick-slip transition is simplified considerably by the knowledge of the precise parameter value where the transition occurs. We also learned that it is necessary to use a very small grid spacing Δx to insure accuracy close to threshold. In contrast to the conclusion of Gnecco *et al.*, we found that $\mathcal{A}$ varies *continuously* as the dimensionless indentation rate α is increased through its critical value α_c. In addition, we determined that $\mathcal{A} \propto (\alpha - \alpha_c)^{1/2}$ for α just above α_c. Analogous results were obtained for the behavior of the ripple amplitude $\mathcal{A}$ as the dimensionless scan velocity r was reduced through its critical value r_c. The experimental results obtained by Gnecco *et al.* seem to be consistent with a continuous change in $\mathcal{A}$ as the threshold for stick-slip motion is crossed. It is important to note, though, that these experimental results are for tip rastering over multiple parallel lines rather than for scanning through a single line.

In the model of Gnecco *et al.*, if the AFM tip is not dragged across the surface, it will sink deeper and deeper into it [9]. In fact, as Eq. (6) shows, the depth of the tip will increase linearly with time. As noted by Gnecco and his coworkers, this is unrealistic because as the tip indents the polymer, the contact area increases, the average pressure decreases, and the indentation rate declines. In accord with this, experiments show that the indentation depth grows in a sublinear fashion and that it may ultimately saturate [9].

To address this issue with the model of Gnecco *et al.*, the indentation rate was taken to be a function of the depth of the tip in Refs. [12] and [13]. In this modified version of the model, Eq. (8) still applies but Eq. (6) is replaced by

$$u_t(x,t) = -\exp(-|u(x_0(t),t)|/b) f(x - x_0(t)), \tag{61}$$

where $u(x_0(t),t)$ is the depth of the tip and $b > 0$ has dimensions of length. If the tip is not dragged, its depth does not saturate after this modification has been made. Instead, it grows logarithmically in time [13].

The change in the model described by Eq. (61) makes analytical work much more challenging because it is no longer possible to write down a closed equation that governs the dynamics of the tip position when v_0 is nonzero. In this paper, therefore, we elected to study the unmodified model, *i.e.*, the limit in which $b = \infty$. It is natural to ask when the unmodified model is a good approximation to the dynamics.

Equation (61) makes it clear that the unmodified model is a good approximation if the ripple amplitude $\mathcal{A}$ is small compared to b. As we have seen, $\mathcal{A}$ is small or zero close to the transition to stick-slip motion. The unmodified model can therefore be safely applied in that regime.

VIII. CONCLUSIONS

In this paper, we studied the patterns produced by dragging an AFM tip over a compliant surface using a mesoscopic, phenomenological model introduced by Gnecco *et al.* [9]. We showed that the problem can be reduced to solving a closed integro-differential equation for a single degree of freedom, the position of the AFM tip. The equation of motion depends on just two parameters: the dimensionless indentation rate α and the dimensionless velocity of the rigid support r. We found the steady-state solution to this equation and then carried out a linear stability analysis of it. This yielded a closed equation that can be solved for the critical value of either α or r. If the steady-state motion is perturbed, so long the deviation from the steady state is small, the deviation of the tip's position from the steady state can be written as a linear superposition of terms of the form $\exp(\lambda_k t)$, where the complex constants λ_k are solutions to an integral equation. For α greater than the critical value α_c, periodic stick-slip motion sets in after a transient. Our simulations show that the amplitude of these oscillations grows as $(\alpha - \alpha_c)^{1/2}$ for α just above α_c. In addition, a pair of λ_k's that are complex conjugates of each other have a real part that changes sign from negative to positive as α is increased through its critical value. This means that the transition from steady-state to periodic stick-slip motion is a supercritical Hopf bifurcation. Analogous statements can be made about the behavior if r is reduced below its critical value r_c and α is held fixed. Finally, we established that the results we obtained for the 2D model of Gnecco *et al.* carry over in a straightforward fashion to the generalization of the model to 3D.

The work described in this paper pertains to a single line scan of the AFM tip over a

polymer surface. The advances made in this paper should allow fresh progress to be made on the problem of the ripples formed by rastering the AFM tip over the surface in a sequence of parallel lines. This will be the subject of our future work in this field.

Appendix

Suppose the system is in its steady state for $t < 0$. Then, starting at time $t = 0$, a weak external force $\mathcal{F}_{\rm ext}(t)$ is briefly applied. In this Appendix, we will show that shortly after the steady state has been disturbed, the deviation from the steady state $l_1(t) = l(t) - l_0$ can be written as a linear superposition of solutions of the form (28) where the λ's are solutions to Eq. (29).

$l_1(t)$ is small for sufficiently small times t because the applied external force is weak. We can therefore discard terms of second and higher order in l_1 in the equation of motion (17). This gives

$$\dot{l}_1(t) = \int_0^\infty F'(r\tau) l_1(t-\tau) d\tau - l_1(t) - \mathcal{F}_{\rm ext}(t), \tag{A.1}$$

which naturally reduces to Eq. (26) when there is no external force. For convenience, we set $K(\tau) \equiv F'(r\tau)$. We also let $t' = t - \tau$. Equation (A.1) becomes

$$\dot{l}_1(t) = \int_{-\infty}^t K(t-t') l_1(t') dt' - l_1(t) - \mathcal{F}_{\rm ext}(t). \tag{A.2}$$

Because $\mathcal{F}_{\rm ext}(t) = 0$ for $t < 0$, the deviation from the steady state $l_1(t)$ must also vanish for $t < 0$. Equation (A.2) therefore reduces to

$$\dot{l}_1(t) = \int_0^t K(t-t') l_1(t') dt' - l_1(t) - \mathcal{F}_{\rm ext}(t). \tag{A.3}$$

Notice that the integral that appears on the right-hand side of Eq. (A.3) is the convolution of K and l_1.

Our next step will be to take the Laplace transform of Eq. (A.3) and apply the convolution theorem. This gives

$$s\tilde{l}_1(s) = \tilde{K}(s)\tilde{l}_1(s) - \tilde{l}_1(s) - \tilde{\mathcal{F}}_{\rm ext}(s), \tag{A.4}$$

where, for an arbitrary function $h(t)$,

$$\tilde{h}(s) \equiv \int_0^\infty e^{-st} h(t) dt \tag{A.5}$$

i.e., $\tilde{h}(s)$ denotes the Laplace transform of $h(t)$. Solving Eq. (A.4) for $\tilde{l}_1(s)$ yields

$$\tilde{l}_1(s) = \frac{\tilde{\mathcal{F}}_{\rm ext}(s)}{\tilde{K}(s) - s - 1}. \tag{A.6}$$

Our final step is to invert the Laplace transform and so obtain $l_1(t)$ for $t \geq 0$. Let the roots of $\tilde{K}(s) - s - 1$ be λ_1, $\lambda_2, \ldots$ and λ_n. We select a real number γ that is greater than $\mathrm{Re}\,\lambda_1$, $\mathrm{Re}\,\lambda_2 \ldots$ and $\mathrm{Re}\,\lambda_n$. Then, according to Mellin's inverse formula,

$$l_1(t) = \frac{1}{2\pi i} \lim_{T\to\infty} \int_{\gamma - iT}^{\gamma + iT} e^{st} \frac{\tilde{\mathcal{F}}_{\rm ext}(s)}{\tilde{K}(s) - s - 1} ds. \tag{A.7}$$

If the integrand in Eq. (A.7) falls to zero with sufficient rapidity as $|s| \to \infty$, we can close the contour and apply the residue theorem. This gives

$$l_1(t) = \sum_{k=1}^{n} \mathrm{Res}\left(e^{st} \frac{\tilde{\mathcal{F}}_{\rm ext}(s)}{\tilde{K}(s) - s - 1}, \lambda_k \right), \tag{A.8}$$

where $\mathrm{Res}(h(s), \lambda)$ denotes the residue of $h(s)$ at the point $s = \lambda$. Assuming that the poles are all of order 1, we obtain

$$l_1(t) = \sum_{k=1}^{n} \frac{\tilde{\mathcal{F}}_{\rm ext}(\lambda_k)}{\tilde{K}'(\lambda_k) - 1} e^{\lambda_k t}. \tag{A.9}$$

($l_1(t)$ can also be written as a linear superposition of $e^{\lambda_1 t}$, $e^{\lambda_2 t} \ldots$, and $e^{\lambda_n t}$ if one or more of the poles is not of order 1.) A solution λ of the equation $\tilde{K}(\lambda) - \lambda - 1 = 0$ satisfies Eq. (29). Thus, the deviation from the steady state $l_1(t)$ can be written as a linear combination of solutions of the form (28) where the λ's are solutions to Eq. (29), as claimed.

ACKNOWLEDGMENTS

We are grateful to Enrico Gnecco and Juan J. Mazo for valuable discussions and correspondence. We are also indebted to Prof. Gnecco for his critical comments on the manuscript. This work was supported by Grants DMS-1814941 and DMR-2116753 awarded by the U.S. National Science Foundation.

---

[1] O. M. Leung and M. C. Goh, Science **255**, 64 (1992).

[2] Z. Elkaakour, J. Aime, T. Bouhacina, C. Odin, and T. Masuda, Phys. Rev. Lett. **73**, 3231 (1994).

[3] R. H. Schmidt, G. Haugstad, and W. L. Gladfelter, Langmuir **19**, 898 (2003).

[4] R. Leach, F. Stevens, C. Seiler, S. Langford, and J. Dickinson, Langmuir **19**, 10225 (2003).

[5] M. D'Acunto, S. Napolitano, P. Pingue, P. Giusti, and P. Rolla, Materials Letters **61**, 3305 (2007).

[6] E. Gnecco, E. Riedo, W. P. King, S. R. Marder, and R. Szoszkiewicz, Phys. Rev. B **79**, 235421 (2009).

[7] S. Napolitano, M. D'Acunto, P. Baschieri, E. Gnecco, and P. Pingue, Nanotechnology **23**, 475301 (2012).

[8] Y. Yan, Y. Sun, J. Li, Z. Hu, and X. Zhao, Nanoscale Research Letters **9**, 1 (2014).

[9] E. Gnecco, P. Pedraz, P. Nita, F. Dinelli, S. Napolitano, and P. Pingue, New Journal of Physics **17**, 032001 (2015).

[10] P. Pedraz, R. Wannemacher, and E. Gnecco, ACS Nano **9**, 8859 (2015).

[11] Y. Yan, X. Cui, Y. Geng, and Y. He, Micro & Nano Letters **12**, 1011 (2017).

[12] J. J. Mazo, P. J. Martínez, P. Pedraz, J. Hennig, and E. Gnecco, Phys. Rev. Lett. **122**, 256101 (2019).

[13] P. J. Martínez, E. Gnecco, and J. J. Mazo, Phys. Rev. E **103**, 022802 (2021).

[14] S. Strogatz, *Nonlinear Dynamics and Chaos: with Applications to Physics, Biology, Chemistry, and Engineering* (Westview Press, Boulder, CO, 2015).